Materials Today 99 (2026) 103448

Contents lists available at ScienceDirect

Materials Today

journal homepage: www.elsevier.com/locate/mattod

# Revealing the spin structure, exchange constants and local anisotropy in nanoparticles with polarised neutron powder diffraction: $Mn_3O_4$ as case study

I.A. Kibalin [a], A. Gukasov [b], I.V. Golosovsky [c], A.G. Roca [d], A. López-Ortega [e,f], M. Estrader [g,h], T.C. Hansen [i], I. Puente-Orench [i,j], E. Lelièvre-Berna [i], J. Nogués [d,k,*]

[a] Data Management and Scientific Computing, European Spallation Source ERIC, Asmussens Allé 305, 2800 Kongens Lyngby, Denmark
[b] Laboratoire Léon Brillouin, CEA-CNRS, CE-Saclay, 91191 Gif-sur-Yvette, France
[c] National Research Center "Kurchatov Institute", B. P. Konstantinov Petersburg Nuclear Physics Institute, 188300 Gatchina, Russia
[d] Catalan Institute of Nanoscience and Nanotechnology (ICN2), CSIC and BIST, Campus UAB, Bellaterra E-08193 Barcelona, Spain
[e] Departamento de Ciencias, Universidad Pública de Navarra, 31006 Pamplona, Spain
[f] Institute for Advanced Materials and Mathematics INAMAT$^2$, Universidad Pública de Navarra, 31006 Pamplona, Spain
[g] Departament de Química Inorgànica i Orgànica, Universitat de Barcelona, Diagonal 645, 08028 Barcelona, Spain
[h] Institute of Nanoscience and Nanotechnology of the University of Barcelona (IN2UB), Spain
[i] Institut Laue Langevin, 71 avenue des Martyrs, 38000 Grenoble, France
[j] Instituto de Nanociencia y Materiales de Aragón, Pedro Cerbuna 12, 50009 Zaragoza, Spain
[k] ICREA, Pg. Lluis Companys 23, E-08010 Barcelona, Spain

ARTICLE INFO

*Keywords:*
Polarised neutron powder diffraction
$Mn_3O_4$ nanoparticles
Exchange constants
Local anisotropy

ABSTRACT

The functional magnetic properties of nanostructured materials can be distinctly different from their bulk counterparts. Understanding these properties is crucial for basic material science and for applications using nanostructured magnetic materials. However, determining intrinsic magnetic structures, exchange constants and local magnetic anisotropy in nanoparticles poses considerable challenges. Here, polarised neutron powder diffraction (PNPD) data, analysed in the frame of the Local Susceptibility and Model Hamiltonian approaches, is used to gain information on the contribution of the different magnetic sublattices on the magnetisation process in $Mn_3O_4$ nanoparticles in unprecedented detail. The magnetic order is found to be a Yafet-Kittel-type canted structure with inter- and intra-sublattice antiferromagnetic couplings, similar to bulk. PNPD corroborates that the c-axis is the hard-axis and the individual contributions of each magnetic site to the easy-plane magnetic anisotropy are determined. Remarkably, the analysis of the PNPD data provides the foremost determination of the microscopic magnetic parameters in nanoparticles, namely, intra- and inter- sub-lattice exchange constants and the local anisotropy parameter. The obtained values are consistent with bulk $Mn_3O_4$ experimental and theoretical results. These results open the path for the use of PNPD to gain unique magnetic information in nanostructured materials, particularly in complex, novel, or poorly understood systems.

## Introduction

Nanostructured magnetic materials are generating enormous interest both due to their novel properties and the broad range of applications in very widespread fields (e.g., permanent magnets, magnetocalorics, theranostics, terahertz applications, or recording media, to mention a few) [1–3]. It is well known that the magnetic response of nanostructured systems can be quite different from that of their bulk counterparts. Apart from the conventional consequences arising from finite size, like superparamagnetism or surface anisotropy [1–4], more profound phenomena often take place in the magnetic order as the size of the nanostructures decreases [3,5–20]. Diverse effects, such as non-collinear structures, spin reorientation, suppression of bulk magnetic spin arrangements or the emergence of magnetic structures not existing in bulk, among others, have been reported for magnetic nanoparticles [3,5–20]. These changes in the magnetic order can have a significant

* Corresponding author at: Catalan Institute of Nanoscience and Nanotechnology (ICN2), CSIC and BIST, Campus UAB, Bellaterra, E-08193 Barcelona, Spain.
*E-mail address:* josep.nogues@icn2.cat (J. Nogués).

https://doi.org/10.1016/j.mattod.2026.103448
Received 21 January 2026; Received in revised form 29 April 2026; Accepted 3 July 2026
Available online 16 July 2026

effect on the functional properties of the nanoparticles (e.g., saturation magnetisation, anisotropy, or coercivity), which, in turn, are crucial for different applications. Thus, understanding these changes in the fundamental magnetic properties as the size decreases is key to progress towards more efficient applications of nanostructured magnetic materials.

Notably, finding the spin structure of nanostructured systems, particularly in the presence of an applied field, is not straightforward. Limited information of the magnetic arrangements in nanoparticles can be obtained by diverse techniques like small angle neutron scattering, Mössbauer spectroscopy, X-ray magnetic circular dichroism, magnetometry, nuclear resonant scattering, or nuclear magnetic resonance [6,12,13,17,21–23]. Nevertheless, most of these techniques only render partial or indirect information. In bulk powdered materials spin structures are traditionally obtained by neutron powder diffraction or polarised neutron powder diffraction [5,7,9,13,16–20]. However, due to the small particle size the neutron diffraction peaks of nanostructured systems are rather broad, leading to a severe overlap between peaks impeding the accurate determination of the magnetic order. Similarly, obtaining comprehensive information on some functional properties in nanostructured systems, such as the intrinsic magnetic anisotropy, can be hindered by diverse factors like the random distribution of the particles, surface and interface effects or the interaction between particles [4,24,25]. Finally, exchange constants give information about the strength and direction coupling between magnetic moments in magnetic materials, which is key to understanding the basic properties of magnetic materials [26]. These constants are experimentally obtained by, for example, fitting the temperature dependence of the magnetisation or the inverse susceptibility [26] or by inelastic scattering [27]. However, the magnetisation and susceptibility approaches cannot be used in nanostructured materials due to the strong contributions of superparamagnetism, dipolar interactions and surface effects. Additionally, due to their complexity, inelastic scattering experiments in nanoparticles are very rare [28], and consequently, there is virtually no information of exchange constants in nanoparticles. Hence, novel approaches are required to accurately investigate the intrinsic magnetic properties of nanostructured materials.

Here, polarised neutron powder diffraction (PNPD), analysed in the framework of new Model Hamiltonian approach is used to quantitatively determine with unparalleled detail the fundamental magnetic characteristics of $Mn_3O_4$ nanoparticles; spin structure, exchange constants and intrinsic local magnetic anisotropy. The obtained results are compatible with values of bulk $Mn_3O_4$. For consistency, the data is also analysed using the conventional, simpler, qualitative Local Susceptibility approach. The overall results of the two approaches agree nicely with each other.

Manganese oxide, $Mn_3O_4$ (hausmannite), has a tetragonal normal spinel crystal structure [space group $I4_1/amd$; see Fig. 1a], with the formula $(Mn^{2+})[Mn^{3+}]_2O_4$, where () and [ ] brackets denote tetrahedral (A) and octahedral (B) sites, respectively. $Mn_3O_4$ nanoparticles have recently become a focus of considerable research interest, driven by their potential use across diverse areas [29,30]. Remarkably, although the basic magnetic properties of $Mn_3O_4$ nanoparticles are well established [31], their magnetic order has not yet been elucidated. The magnetic ground-state of bulk $Mn_3O_4$ at low temperature is a complex canted spin configuration known as Yafet-Kittel-type structure [32]. Although the existence of a Yafet-Kittel-type structure in $Mn_3O_4$ is well accepted, the details of its magnetic configuration are not completely determined. Due to the symmetry of the magnetic structure, unpolarised neutron diffraction cannot distinguish some of the details of the magnetic order in $Mn_3O_4$ and several arrangements of the $Mn^{3+}$ moments have been proposed [33–36]. Similarly, the details of the large anisotropy of $Mn_3O_4$ remain unclear. For example, an easy-axis anisotropy along the *c*-axis of $Mn^{3+}$ [37] or an easy *ab*-plane anisotropy of $Mn^{2+}$ ions [38] have been proposed. The complex magnetic structure of $Mn_3O_4$ and its non-trivial anisotropy, make $Mn_3O_4$ nanoparticles a perfect candidate to highlight the enormous potential of the Model Hamiltonian approach applied to polarised neutron powder diffraction data.

## Results and discussion

### *$Mn_3O_4$ nanoparticles basic characterisation*

$Mn_3O_4$ nanoparticles (see Experimental Section) with transmission electron microscopy sizes of 11(2) nm (sample 1) and 13(2) nm (sample 2) have been studied (Fig. S1).

The average crystallite sizes estimated from the unpolarised neutron diffraction peak broadening were 9.4(5) nm (sample 1) and 8.8(5) nm (sample 2), respectively. Similar crystallite sizes were deduced from the X-ray diffraction data (Fig. S2), which were consistent with the TEM results.

### *$Mn_3O_4$ ground-state magnetic structure*

The profile refinement of the unpolarised neutrons and X-ray diffraction patterns (Fig. 1b and Fig. S2) showed that the studied nanoparticles exhibit a tetragonal spinel structure, similar to that of bulk $Mn_3O_4$ [33–35]. The analysis also confirmed a chemical composition close to stoichiometric hausmannite with $Mn^{2+}$ and $Mn^{3+}$ ions occupying the tetrahedral (A) and octahedral (B) sites, respectively. The lattice parameters of the samples are consistent with those reported for bulk $Mn_3O_4$ [39].

The magnetic structure of bulk $Mn_3O_4$ at low temperature has previously been determined with unpolarised neutron diffraction [33–35]. It corresponds to a non-collinear Yafet-Kittel type configuration, which can be described by a tetragonal unit cell doubled along the b-axis. In this structure, $Mn^{2+}$ spins align ferromagnetically along the b-axis,

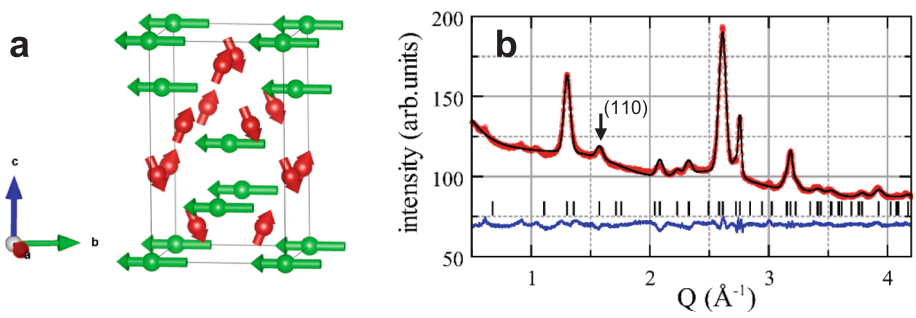


**Fig. 1.** Magnetic structure and unpolarised powder diffraction pattern and of $Mn_3O_4$. (a) Commensurate Yafet-Kittel-type magnetic structure obtained in the refinement; The moments and atoms in the tetrahedral A- ($Mn^{2+}$, 4.57$\mu_B$) and the octahedral B-sites ($Mn^{3+}$, 2.43(5)$\mu_B$) are shown in green and red, respectively. (b) Powder neutron diffraction at 5 K for sample 1. The red symbols are the experimental data, the black line is the refinement and the blue line is the difference between the experimental and refined profiles. The vertical bars show the position of the reflections. The arrow highlights the magnetic reflection (110).

while the $Mn^{3+}$ spins at the octahedral sites, lying in the (bc)-plane, are symmetrically canted with respect to the b-axis forming the Yafet-Kittel angle $\theta_{YK}$.

Due to the low diffraction signal from nanoparticle samples, the refinement of the unpolarised neutron powder diffraction patterns collected at 5 K cannot distinguish between the reported models [33–35], all of them describing the diffraction profile reasonably well. The Yafet-Kittel non-collinearity is clearly evidenced by the presence of the (110) magnetic reflection in the diffraction pattern (indicated by the black arrow in Fig. 1b), which is forbidden in collinear spin structures. However, in contrast to bulk $Mn_3O_4$, no satellite peaks associated with the propagation vector (0 ½ 0) were observed within the limits of our experimental precision (Fig. S3a).

Consequently, the final refinement was performed assuming a commensurate magnetic structure without subdivision into R- and S-sublattices for $Mn^{3+}$ ions at the octahedral site (B-site) (see Supporting Information 2). With the $Mn^{2+}$ moment fixed at 4.57 $\mu_B$ and the Yafet-Kittel angle set to 67° (like in bulk), the refined magnetic moment of $Mn^{3+}$ at the B-site was determined to be 2.43(5)$\mu_B$ (Fig. 1a).

Thus, the refined structure of the $Mn_3O_4$ nanoparticles (Fig. 1a) resembles the spin arrangement in the bulk material [33–35] but the temperature dependence of the magnetic moment in the nanoparticles differs from that of the bulk. Indeed, in contrast to the sharp decrease in magnetic scattering at $T_N \sim 45$ K observed in bulk [34], the nanoparticles exhibit persistent magnetic scattering well above the transition temperature (Fig. S4).

### *$Mn_3O_4$ magnetic structure in external magnetic field*

To elucidate the evolution of the $Mn_3O_4$ magnetic structure under applied magnetic fields, PNPD measurements were performed at various field strengths. With this technique, the spin-dependent scattering cross-sections are measured using an incident neutron beam polarised either parallel ($I^+$) or antiparallel ($I^-$) to the applied magnetic field [40,41].

Fig. 2a displays the sum ($I^+ + I^-$) and difference ($I^+ - I^-$) diffraction patterns collected at 5 K for sample 2 under magnetic fields of 5 and 50 kOe. The data was analysed using two complementary approaches: the well-established Local Magnetic Susceptibility method [40–46] and a newly developed Model Hamiltonian framework incorporating isotropic exchange interactions, uniaxial anisotropy, and Zeeman energy terms (see Supporting Information 6). Note that the both refinements were carried out without subdivision into R- and S-sublattices for the $Mn^{3+}$ ions at the octahedral sites (B-site) (see Supporting Information 2).

### *Local Susceptibility approach*

The Rietveld refinement, carried out using the CrysPy package [44] within the Local Susceptibility approach, yields an excellent fit to both the sum and difference profiles (Fig. 2a). The resulting magnetisation ellipsoids —graphical representations of the local susceptibility tensors [40]— are shown in Fig. 2b for the manganese ions in the unit cell, as refined from data collected under applied magnetic fields of 5 and 50 kOe. These ellipsoids describe surfaces where each radius vector corresponds to a magnetic moment **m** induced by an applied field **H** of fixed magnitude and arbitrary direction. The principal axes of the ellipsoids define the directions of magnetic anisotropy, where the longest axis

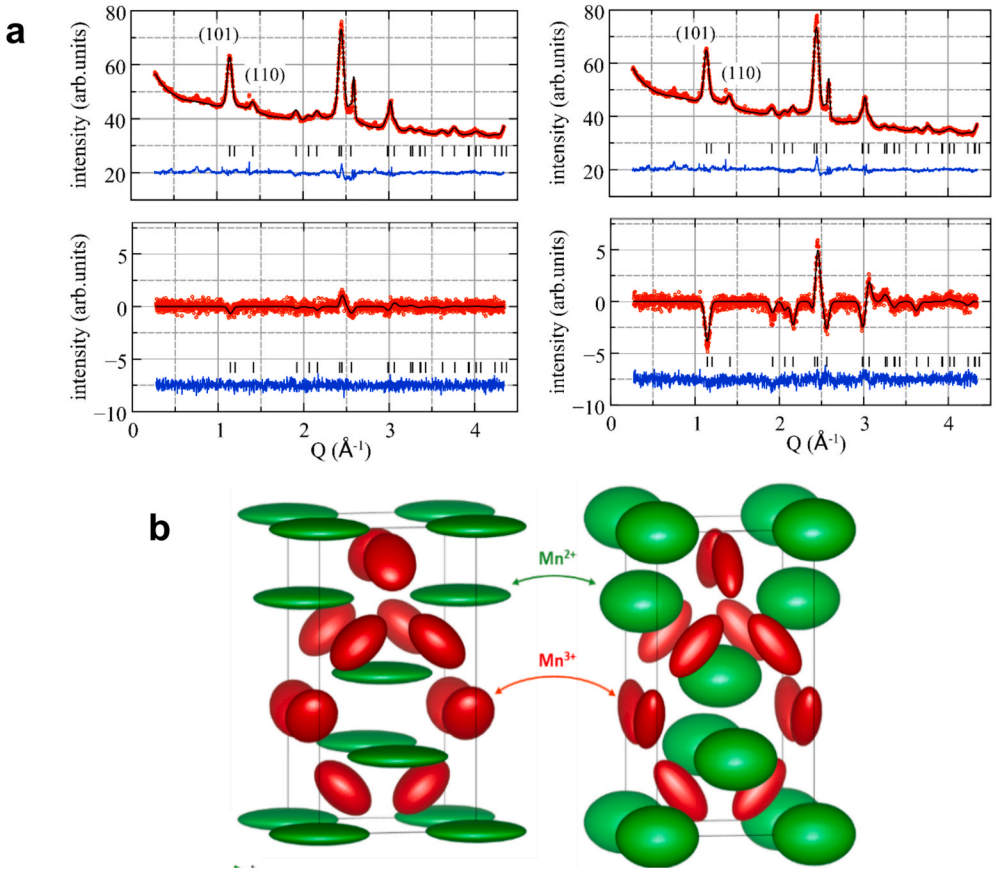


**Fig. 2. PNPD profiles refined using the Local Susceptibility approach and magnetic ellipsoidsof $Mn_3O_4$.** (a) Rietveld refinement of sum ($I^+$+$I^-$; top) and difference ($I^+$-$I^-$; bottom) PNPD patterns at 5 K in fields of 5 kOe (left) and 50 kOe (right) performed using the CrysPy package [44] within the local susceptibility approach. The vertical bars show the position of the reflections. (b) The resulting magnetization ellipsoids, graphical representations of the local susceptibility tensors [41]] for the manganese ions in the unit cell, refined from data collected under applied magnetic fields of 5 kOe (left) and 50 kOe (right).

denotes the local easy axis, while the shortest indicates the hard axis. Importantly, unlike conventional magnetometry, which provides a response averaged over the unit cell, PNPD yields the anisotropy at each crystallographic magnetic site.

At 5 kOe, the A-site ellipsoids exhibit a distinctly oblate shape, indicating that the $Mn^{2+}$ moments are primarily induced within the *ab*-plane, independent of the field orientation. This behaviour is consistent with earlier neutron diffraction [34] and NMR [37] studies on single crystals. However, there is a debate about the microscopic origin of the bulk anisotropy in $Mn_3O_4$. For example, an easy-axis anisotropy along the *c*-axis of $Mn^{3+}$ [38] or an easy *ab*-plane anisotropy of $Mn^{2+}$ ions [37] have been proposed. In the latter case, the $Mn^{3+}$ moments would lie in the *ab*-plane at low fields. The orientation of the $Mn^{3+}$ magnetisation ellipsoids axes shown in Fig. 2a,b contradicts this hypothesis. Fig. 2a,b also show that the in-plane anisotropy of the $Mn^{2+}$ ions (green ellipsoids) decreases at high fields (50 kOe), while the axial anisotropy of the $Mn^{3+}$ ions (red ellipsoids) remains roughly independent of the field. Thus, the anisotropy of the $Mn^{3+}$ ions is at the microscopic origin of the bulk anisotropy in $Mn_3O_4$.

At 50 kOe, the applied field is sufficient to overcome the local anisotropy, enabling substantial moment induction along the hard *c*-axis when the field is aligned in that direction. Furthermore, the analysis of the collective ellipsoid orientations indicates that the *c*-axis is the global hard magnetisation axis in $Mn_3O_4$ nanoparticles, in agreement with angular-dependent bulk magnetometry measurements [47].

Additionally, it is observed that the easy anisotropy axes of some B-sites make an angle of approximately 44° with respect to the *c*-axis. This canting angle is notably smaller than the previously reported Yafet-Kittel angle of 65–70° [34] for the bulk material, and also smaller than the value obtained from our unpolarised neutron diffraction data on $Mn_3O_4$ nanoparticles in zero field. The discrepancy arises from the inherent limitations of the Local Susceptibility approach when applied to magnetically ordered states, where exchange interactions are non-negligible.

The magnitudes of the induced magnetic moments at both A- and B-sites can be extracted through diagonalisation of the magnetisation tensors (see Supporting Information 4). For the A-sites, the moment magnitude under an applied field of 50 kOe is 4.4(2) $\mu_B$ closely matching the ordered moment of 4.3(1) $\mu_B$ for $Mn^{2+}$ as determined from zero-field neutron diffraction on bulk samples [34]. For the B-sites, the moment of 3.63(6) $\mu_B$ is consistent with the expected value for $Mn^{3+}$ ions and agrees well with results from unpolarised neutron diffraction [33]. These findings unequivocally confirm that $Mn^{2+}$ ions occupy the A-sites, while $Mn^{3+}$ ions reside on the B-sites.

Notably, one of the eigenvalues associated with the $Mn^{3+}$ susceptibility tensor is negative relative to the field direction (Table S1). This indicates that, depending on the orientation of the applied field with respect to the crystallite axes, the $Mn^{3+}$ moments can align either parallel or antiparallel to the field. Such behaviour provides evidence of competing magnetic interactions within the system. In particular, it suggests the presence of antiferromagnetic exchange coupling between $Mn^{3+}$ and $Mn^{2+}$ ions, which is consistent with the formation of non-collinear spin configurations characteristic of Yafet–Kittel-type structures [32].

According to the definition of the susceptibility tensor, the sum of the local susceptibilities across all magnetic ions within the unit cell should correspond to the bulk magnetic susceptibility. To assess the internal consistency of the Local Susceptibility model, the unit cell–averaged magnetisation was computed from the magnetisation ellipsoids at various field strengths. Remarkably, these calculations show excellent agreement with bulk magnetometry measurements conducted on sample 2 (see Fig. S5).

It is important to note that the Local Susceptibility approach is formally valid only in the paramagnetic regime and under weak magnetic fields. Nevertheless, our results demonstrate that, even when applied to magnetically ordered states, this method captures in a fast and convenient way the key features of field-induced magnetic behaviour (e.g., easy axes and relative anisotropy [48]). While the Local Susceptibility approach can be extended to reconstruct the distribution of magnetic moments (see Supporting Information 7), it does not provide access to microscopic magnetic parameters. To address this limitation, a new approach based on a Model Hamiltonian has been developed for analysing PNPD data to enable the quantitative determination of microscopic magnetic parameters, including sublattice moments, exchange constants, and local magnetic anisotropy energies, thereby offering a more comprehensive description of the field evolution of magnetic structures in nanostructured materials.

### *Model Hamiltonian approach*

To refine the PNPD data beyond the limitations of the Local Susceptibility model, a classical spin Hamiltonian closely related to that previously used in linear spin-wave calculations [49] was adopted. This Hamiltonian accounts for the essential microscopic interactions governing the magnetic behaviour of $Mn_3O_4$ and includes the following contributions: the isotropic Heisenberg exchange interaction between moments at the A- and B-sites (denoted $J_{AB}$) and exchange interaction between moments in the B-sites ($J_{BB}$), and the single-ion anisotropy at the B-site $D_B^z$, where *z* represents the axis of the anisotropy $\boldsymbol{e}_z$.

The free energy of this system in an external field **H** is expressed as follows:

$$E = -\sum_{i}^{A,B1,B2} \boldsymbol{H}\cdot\boldsymbol{m}_i + 6J_{AB}\sum_{i}^{B1,B2} \boldsymbol{m}_A\cdot\boldsymbol{m}_i + 2J_{BB}\boldsymbol{m}_{B1}\cdot\boldsymbol{m}_{B2} + D_B^z\sum_{i}^{B1,B2}(\boldsymbol{m}_i\cdot\boldsymbol{e}_z)^2 \quad (1)$$

Here, $\mathbf{m}_A$ and $\mathbf{m}_{B1,B2}$ denote the magnetic moments associated with the A- and B-sites, respectively. In the frame of this model one can find the set of magnetic moments $\mathbf{m}_A$, $\mathbf{m}_{B1}$, $\mathbf{m}_{B2}$ that minimises the free energy E, given a set of parameters ($J_{AB}$, $J_{BB}$, $D_B^z$, $m_A$, $m_{B1}$, $m_{B2}$ and the external field value *H*).

The refinement was carried out simultaneously on the sum and difference profiles of datasets collected under applied magnetic fields of 5 kOe and 50 kOe (Fig. 3). Performing a joint refinement across both low- and high-field data is crucial for robust parameter determination, as the low-field measurements are more sensitive to inter-site exchange interactions, and the high-field data predominantly reflect single-ion anisotropy effects (see Supporting Information 6 for further details on the refinement procedure). The refinement yields the following parameters.

$$\widetilde{D}_B^z = m_B\cdot D_B^z = -0.18(5)\text{meV}$$

$$\widetilde{J}_{AB} = \sqrt{m_A m_B}\cdot J_{AB} = 1.50(2)\text{meV}$$

$$\widetilde{J}_{BB} = m_B\cdot J_{BB} = 6.27(5)\text{meV}$$

$$m_A = 5.43(4)\mu_B$$

$$m_{B1,B2} = 3.27(3)\mu_B$$

Remarkably, these values are consistent with the values of bulk $Mn_3O_4$ obtained by density functional theory calculations [50] and from inelastic scattering neutron scattering experiments [49], particularly considering possible deviations in the magnetic structure of nanoparticles compared to bulk $Mn_3O_4$. Importantly, the positive value of $J_{AB}$ implies an antiferromagnetic coupling between the octahedral $Mn^{3+}$ ions B-sublattice and the tetrahedral $Mn^{2+}$ A-lattice sublattice, in agreement with the susceptibility tensor obtained from the Local Susceptibility approach. Similarly, the positive value of $J_{BB}$ indicates that the intrasublattice coupling in the B-sublattice is also antiferromagnetic.

In the initial formulation of the Hamiltonian, several additional

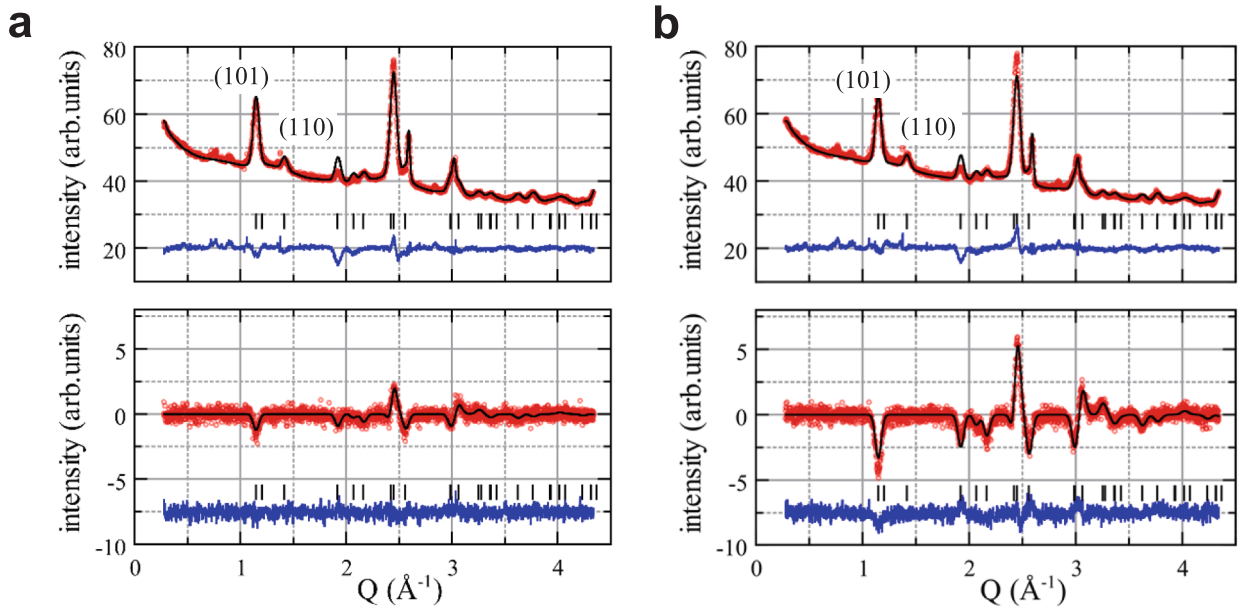


**Fig. 3.** PNPD profiles refined using the Model Hamiltonian approach. Sum ($I^+ + I^-$; top) and difference ($I^+ - I^-$; bottom) profiles measured at temperature 5 K in fields (a) 5 and (b) 50 kOe for sample 2 and refined together with the parameters of the model described by Eq. (1). The red symbols are the experimental data, the black line is the refinement, and the blue line is the difference between the experimental and refined profiles. The vertical bars show the position of the reflections.

terms were included: the exchange interaction between A-site moments ($J_{AA}$), the interaction between inequivalent B-site moments ($J_{BB'}$), and the single-ion anisotropy at the A-sites ($D_A$). These terms were subsequently excluded from the refinement because their contributions were found to be negligible, consistent with experimental and theoretical results [49,50]. Their removal helped reduce the number of free parameters and improved the robustness of the fit.

From the value of $\widetilde{D}_B^z$, the contribution of the B-sites to the bulk magnetic anisotropy can be estimated, yielding $K_c \sim -1.28$ meV (i.e., $-1.2 \times 10^7$ erg/cm$^3$). Considering that the dominant source of magnetic anisotropy arises from the $Mn^{3+}$ ions at the B-sites (as discussed above), this estimated $K_c$ is in a good agreement with the experimentally determined c-axis anisotropy in bulk $Mn_3O_4$ ($K_c = -1.6 \times 10^7$ erg/cm$^3$) [51].

Using the refined Hamiltonian parameters, it is possible to calculate the magnetic structure of a single crystallite subjected to an external magnetic field applied in an arbitrary direction, corresponding to various crystallite orientations within a polycrystalline sample. As an illustrative example, Fig. 4a shows the magnetic configurations induced by a 50 kOe field applied along the b-axis ([010] direction). In this orientation, the resulting non-collinear arrangement of the magnetic moments largely retains the key features of the Yafet-Kittel ground state.

Fig. 4b schematically illustrates the distribution of magnetic moments at the A- and B-sites, calculated using the parameters obtained from the Model Hamiltonian approach for an applied magnetic field of 50 kOe rotating within the *bc*-plane. It is important to emphasise that all spin configurations depicted in the figure are expected to be present in the sample, as it consists of randomly oriented nanoparticles.

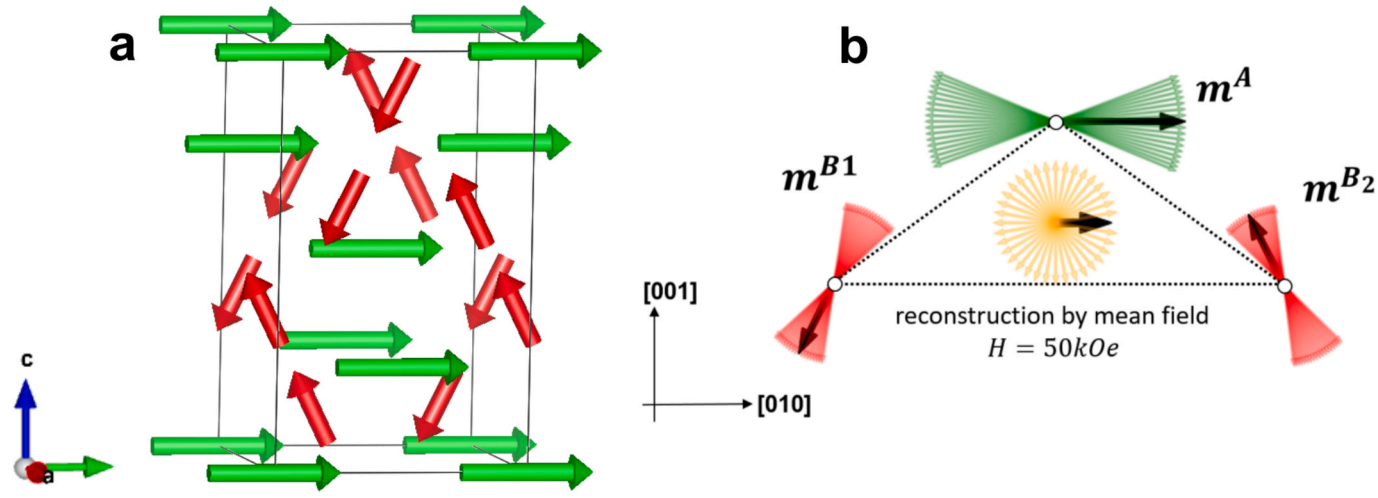


**Fig. 4.** Magnetic structures of $Mn_3O_4$ powder in field reconstructed using the Model Hamiltonian approach. (a) Magnetic moment configurations induced by an applied magnetic field of 50 kOe along the b-axis, calculated using the refined parameters from the Model Hamiltonian approach. (b) Schematic representation of the magnetic moment distribution at the A-sites (green arrows) and B-sites (red arrows) under rotation of the magnetic field within the bc-plane (yellow arrows). The black arrows indicate the moment orientation for a representative crystallite with the external field aligned along the b-axis. B1 and B2 denote two symmetry-equivalent positions within the B-site sublattice.

Interestingly, in contrast to the Local Susceptibility approach, the canting angle, as derived from the Model Hamiltonian, is found to be approximately 62(4)°, in close agreement with the Yafet-Kittel angle characterising the ground state of $Mn_3O_4$.

## Conclusion

To summarise, a detailed study of $Mn_3O_4$ nanoparticles was carried out using both polarised and unpolarised powder neutron diffraction. The refinement of polarised neutron powder diffraction data with the Local Susceptibility model and a newly developed Model Hamiltonian approach allows to describe the evolution of the non-collinear magnetic structure under applied magnetic fields. The Local Susceptibility analysis has enabled the decomposition of the individual contributions from different magnetic sublattices to the overall magnetic anisotropy. This analysis revealed that the *c*-axis is the hard anisotropy axis and confirmed the presence of easy-plane anisotropy, in agreement with single-crystal magnetometry data for $Mn_3O_4$.

The Model Hamiltonian approach has provided a quantitative framework for determining, for the first time, key magnetic parameters, including inter- and intra-sublattice exchange interactions and site-specific anisotropies, in a nanostructured system, with values consistent with bulk $Mn_3O_4$ experimental and theoretical results.

These findings underscore the great potential of polarised powder neutron diffraction as a tool for probing magnetic structures and local anisotropies in magnetically ordered nanoparticles. In particular, the combination of polarised neutron data with the Model Hamiltonian approach offers a powerful methodology for quantifying exchange couplings and crystal field anisotropies, even in nanoscale or structurally complex materials. This paves the way for the study of emerging and poorly characterised magnetic systems for the development of new types of nanoparticles with tailored properties. Actually, our Model Hamiltonian approach could be extended for the analysis of polarized neutron data of virtually any kind of magnetic material, including bulk polycrystalline materials (using PNPD) or single crystals (using polarized neutron single crystal diffraction). This offers a new approach to obtain the exchange constants parameters not only in nanostructured materials, but in most types of magnetic materials.

## Experimental section

### *Sample preparation*

$Mn_3O_4$ sample 1 was synthesised by thermal decomposition of manganese(II) acetylacetonate in a mixture of oleylamine and dibenzyl ether [52]. Sample 2 was synthesised by thermal decomposition of Mn (II) oleate (which was synthesised previously) in 1-octadecene in the presence of 1-decanol at high temperatures under Ar flow [53].

### *Transmission electron microscopy characterisation*

The morphology of the nanoparticles was characterised by transmission electron microscopy (TEM). The low-resolution measurements were carried out using a JEM-1400 de JEOL, operating at 120 kV, while the high-resolution experiments were performed in a FEI Tecnai G2 F20 HR(S)TEM microscope operated at 200 kV (care was taken to minimise any beam damage on the samples) [54]. The particle size distributions were obtained by counting more than 200 particles and fitting the data to a Gaussian distribution (Fig. S1).

### *X-ray diffraction*

Powder X-ray diffraction patterns were measured at the BL04-beamline at the ALBA Synchrotron (Barcelona, Spain), with a wavelength of 0.4131 Å. All the patterns were refined using the FullProf package [55].

### *Neutron powder diffraction*

The unpolarised powder neutron diffraction experiment of the $Mn_3O_4$ nanoparticles (sample 1) was carried out at the D1B diffractometer of the Institute Laue Langevin (ILL; Grenoble, France) with a neutron wavelength $\lambda = 2.524$ Å. All the patterns were refined using the FullProf package [55].

The polarised neutron powder diffraction data of the $Mn_3O_4$ sample (sample 2) were collected at the D20 diffractometer of the ILL [56]. with incident neutrons of wavelength $\lambda = 2.4$ Å. At D20 the beam was polarised with a $^3$He spin filter [57,58]. The measurements on $Mn_3O_4$ were carried out at 5 K in increasing fields (from 3 to 50 kOe), after zero field cooling. To avoid any rotation of the nanoparticles in the applied field, the powder sample was tightly compacted.

Polarised neutron powder diffraction is based on the measurement of the diffracted intensity for the two polarisation states of the incident neutron beam and can be estimated as

$$y_{\pm} = S\sum\nolimits_h m_h L_f I_{\pm} \psi_h(2\theta - 2\theta_h) + b(2\theta), \quad (4)$$

where $S$ is a scale factor, $m_h$ is the multiplicity of the reflection, $L_f$ is the Lorentz factor, $\psi_h(2\theta - 2\theta_h)$ is the peak profile function normalised to unit area, and b(2θ) is the background. The summation is done over all $h$ reflections for diffraction angles $2\theta$. Because the neutron background from the cryomagnet and the sample holder presented in the diffraction signal $y_{\pm}$ are invariant with the beam polarisation, better quality information can be derived by analysing the difference data $(y_+ - y_-)$ [58]. On the other hand, for scaling the magnetic moment values, a simultaneous refinement of the sum $(y_+ + y_-)$ and difference $(y_+ - y_-)$ of the diffracted intensities is mandatory [44]. The expressions describing the dependence of powder averaged integrated intensities $I_{\pm}$ on the local susceptibility tensors are given in ref. 41. The refinement of the local susceptibility parameters from the sum and difference of the spin-up and spin-down polarised patterns were carried out with the new software package CrysPy [44], specially developed for the Rietveld analysis of polarised neutron powder diffraction data [46].

Note that the small peaks in the diffraction patterns in the range q = 0.6–1.1 $Å^{-1}$ are due to parasitic reflections arising from the sample environment used during the experiments. However, these peaks do not appear in the difference polarized neutron patterns, indicating that these peaks are not magnetic, consequently they do not affect the results presented in the manuscript.

Note that, despite the very small sample volume, in low magnetic fields the incident beam experienced depolarization due to traversing bulk material containing ferrimagnetic nanoparticles with occasionally aligned net magnetization. Therefore, to take this into account, the incident beam depolarization coefficient D was included as a refined parameter. The refinement yielded a rather strong depolarization (D = 0.35) at low fields, 10 kOe, and a much smaller depolarization (D = 0.84) in higher fields, 50 kOe.

### *Magnetisation measurements*

The magnetisation measurements were carried out on tightly packed samples using a superconducting quantum interference device, SQUID, magnetometer (Quantum Design). The temperature dependence of the magnetisation was recorded while warming after zero field cooling from 300 K to 10 K at different applied fields. The hysteresis loops were carried out at 5 K (using a maximum field of 70 kOe) after zero field cooling from 300 K.

### *CRediT authorship contribution statement*

**I.A. Kibalin:** Writing – review & editing, Writing – original draft, Methodology, Investigation, Formal analysis, Conceptualization. **A. Gukasov:** Writing – review & editing, Writing – original draft,

Supervision, Methodology, Investigation, Funding acquisition, Formal analysis, Conceptualization. **I.V. Golosovsky:** Writing – review & editing, Writing – original draft, Supervision, Methodology, Investigation, Funding acquisition, Formal analysis, Conceptualization. **A.G. Roca:** Writing – review & editing, Methodology, Investigation, Funding acquisition. **A. López-Ortega:** Writing – review & editing, Investigation, Funding acquisition. **M. Estrader:** Writing – review & editing, Investigation, Funding acquisition. **T.C. Hansen:** Writing – review & editing, Investigation. **I. Puente-Orench:** Writing – review & editing, Investigation. **E. Lelièvre-Berna:** Writing – review & editing, Investigation. **J. Nogués:** Writing – review & editing, Writing – original draft, Supervision, Funding acquisition, Conceptualization.

## Declaration of competing interest

The authors declare that they have no known competing financial interests or personal relationships that could have appeared to influence the work reported in this paper.

## Acknowledgements

The work was supported by the Russian Foundation for Basic Research under Grant No. 20-02-00109-a and by the European Union's Horizon 2020 research and innovation program under Grant Agreement No. 871072. A.G.R. and J.N. acknowledge financial support from the grants PID2022-138588OB-C32 funded by MCIN/AEI/10.13039/50110001103 and 2021-SGR-00651 from Generalitat de Catalunya. A. G.R. acknowledge financial support from RYC2019-027449-I funded by MCIN/AEI/10.13039/501100011033. ICN2 is funded by the CERCA programme/Generalitat de Catalunya. The ICN2 is supported by the CEX2021-001214-S grant funded by MCIN/AEI/10.13039/501100011033. M.E. acknowledges the grant RYC2018-024396-I funded by MCIN/AEI/ 10.13039/501100011033 and by "ESF Investing in your future" and support from 'Departament de Recerca i Universitats: del Departament d'Acció Climàtica, Alimentació i Agenda Rural i Fons Climàtic de la Generalitat de Catalunya' with the grant 2023CLIMA00022. A.L.O. acknowledges financial support from the grant PID2024-160292OB-I00 funded by MCIN/AEI /10.13039/501100011033/FEDER, EU. The authors thank ILL (D1B doi:10.5291/ILL-DATA.5-31-2650, D20 doi:10.5291/ILL-DATA.5-32-932), and the ALBA Synchrotron for the provision of beam-time.

## Appendix A. Supplementary material

Supplementary data to this article can be found online at https://doi.org/10.1016/j.mattod.2026.103448.

## Data availability

Data will be made available on request.

## References

[1] Z. Ma, J. Mohapatra, K. Wei, J.P. Liu, S. Sun, Chem. Rev. 123 (2023) 3904.
[2] X. Batlle, C. Moya, M. Escoda-Torroella, O. Iglesias, A. Fraile Rodríguez, A. Labarta, J. Mang. Magn. Mater. 543 (2022) 168594.
[3] S. Mørup, E. Brok, C. Frandsen, J. Nanomater. 2013 (2013) 720629.
[4] F. Bødker, S. Mørup, S. Linderoth, Phys. Rev. Lett. 72 (1994) 282.
[5] J.L. García-Muñoz, A. Romaguera, F. Fauth, J. Nogues, M. Gich, Chem. Mater. 29 (2017) 9705.
[6] A.A. Baker, J.R.I. Lee, C.A. Orme, T. Van Buuren, S.K. McCall, J. Phys. Condens. Matter 32 (2020) 495803.
[7] H. Hiraka, K. Ohoyama, Y. Ogata, T. Ogawa, R. Gallage, N. Kobayashi, M. Takahashi, B. Gillon, A. Gukasov, K. Yamada, Phys. Rev. B 90 (2014) 134427.
[8] F. Huang, Z. Wang, X. Lu, J. Zhang, K. Min, W. Lin, R. Ti, T.T. Xu, J. He, C. Yue, J. Zhu, Sci. Rep. 3 (2013) 2907.
[9] E. Brok, K. Lefmann, P.P. Deen, B. Lebech, H. Jacobsen, G.J. Nilsen, L. Keller, C. Frandsen, Phys. Rev. B 91 (2015) 014431.
[10] T.P. Almeida, T. Kasama, A.R. Muxworthy, W. Williams, L. Nagy, T.W. Hansen, P. D. Brown, R.E. Dunin-Borkowski, Nat. Commun. 5 (2014) 5154.
[11] Y. Gao, Y. Bao, A.B. Pakhomov, D. Shindo, K.M. Krishnan, Phys. Rev. Lett. 96 (2006) 137205.
[12] J.A. De Toro, M. Vasilakaki, S.S. Lee, M.S. Andersson, P.S. Normile, N. Yaacoub, P. Murray, E.H. Sánchez, P. Muñiz, D. Peddis, R. Mathieu, K. Liu, J. Geshev, K. N. Trohidou, J. Nogues, Chem. Mater. 29 (2017) 8258.
[13] A.G. Roca, I.V. Golosovsky, E. Winkler, A. López-Ortega, M. Estrader, R.D. Zysler, M.D. Baró, J. Nogues, Small 14 (2018) 1703963.
[14] A. Rathi, P.D. Babu, P.K. Rout, V.P.S. Awana, V.K. Tripathi, R. Nagarajan, B. Sivaiah, R.P. Pant, G.A. Basheed, J. Magn. Magn. Mater. 474 (2019) 585.
[15] B. Belec, G. Dražić, S. Gyergyek, B. Podmiljšak, T. Goršak, M. Komelj, J. Nogues, D. Makovec, Nanoscale 9 (2017) 17551.
[16] S.E. Inderhees, J.A. Borchers, K.S. Green, M.S. Kim, K. Sun, G.L. Strycker, M. C. Aronson, Phys. Rev. Lett. 101 (2008) 117202.
[17] E. Batsaikhan, C.H. Lee, H. Hsu, C.M. Wu, J.C. Peng, M.H. Ma, S. Deleg, W.H. Li, ACS Omega 5 (2020) 3849.
[18] M. Estrader, A. López-Ortega, I.V. Golosovsky, S. Estradé, A.G. Roca, G. Salazar-Alvarez, L. López-Conesa, D. Tobia, E. Winkler, J.D. Ardisson, W.A.A. Macedo, A. Morphis, M. Vasilakaki, K.N. Trohidou, A. Gukasov, I. Mirebeau, O.L. Makarova, R.D. Zysler, F. Peiró, M.D. Baró, L. Bergström, J. Nogués, Nanocale 7 (2015) 3002.
[19] I.V. Golosovsky, I. Mirebeau, F. Fauth, D.A. Kurdyukov, Y.A. Kumzerov, Solid State Commun. 141 (2007) 178.
[20] E. Brok, K. Lefmann, G.J. Nilsen, M. Kure, C. Frandsen, Phys. Rev. B 96 (2017) 104426.
[21] Y.V. Knyazev, A.I. Chumakov, A.A. Dubrovskiy, S.V. Semenov, I. Sergueev, S. S. Yakushkin, V.L. Kirillov, O.N. Martyanov, D.A. Balaev, Phys. Rev. B 101 (2020) 094408.
[22] S.-J. Lee, S. Lee, New J. Phys. 8 (2006) 98.
[23] S. Disch, E. Wetterskog, R.P. Hermann, A. Wiedenmann, U. Vainio, G. Salazar-Alvarez, L. Bergstrom, T. Brückel, New J. Phys. 14 (2012) 013025.
[24] E.H. Sánchez, M. Vasilakaki, S.S. Lee, P.S. Normile, M.S. Andersson, R. Mathieu, A. López-Ortega, B.P. Pichon, D. Peddis, C. Binns, P. Nordblad, K. Trohidou, J. Nogués, J.A. De Toro, Small 18 (2022) 2106762.
[25] J.D. Agudelo-Giraldo, E. Restrepo-Parra, J. Restrepo, Sci. Rep. 10 (2020) 5041.
[26] C.M. Srivastava, G. Srinivasan, N.G. Nanadikar, Phys. Rev. B 19 (1979) 499.
[27] S.E. Hahn, A.A. Podlesnyak, G. Ehlers, G.E. Granroth, R.S. Fishman, A. I. Kolesnikov, E. Pomjakushina, K. Conder, Phys. Rev. B 89 (2014) 014420.
[28] M. Feygenson, X. Teng, S.E. Inderhees, Y. Yiu, W. Du, W. Han, J. Wen, Z. Xu, A. A. Podlesnyak, J.L. Niedziela, M. Hagen, Y. Qiu, C.M. Brown, L. Zhang, M. C. Aronson, Phys. Rev. B 83 (2011) 174414.
[29] Z. Chen, Z. Jiao, D. Pan, Z. Li, M. Wu, C.-H. Shek, C.M.L. Wu, J.K.L. Lai, Chem. Rev. 112 (2012) 3833.
[30] B. Ding, P. Zheng, P. Ma, J. Lin, Adv. Mater. 32 (2020) 1905823.
[31] E. Winkler, R.D. Zysler, D. Fiorani, Phys. Rev. B 70 (2004) 174406.
[32] Y. Yafet, C. Kittel, Phys. Rev. 87 (1952) 290.
[33] B. Boucher, R. Buhl, M. Perrin, J. Phys. Chem. Solids 32 (1971) 2429.
[34] G.B. Jensen, O.V. Nielsen, J. Phys. C: Sol. State Phys. 7 (1971) 409.
[35] B. Chardon, F. Vigneron, J. Magn. Magn. Mater. 58 (1986) 128.
[36] D.P. Kozlenko, N.T. Dang, S.E. Kichanov, L.T.P. Thao, A.V. Rutkauskas, E.V. Lukin, B.N. Savenko, N. Tran, D.T. Khan, L.V. Truong-Son, L.H. Khiem, B.W. Lee, T. L. Phan, N.L. Phan, N. Truong-Tho, N.N. Hieu, T.A. Tran, M.H. Phan, Phys. Rev. B 105 (2022) 094430.
[37] C. Kim, E. Jo, B. Kang, S. Kwon, S. Lee, J.H. Shim, T. Suzuki, T. Katsufuji, Phys. Rev. B 86 (2012) 224420.
[38] O.V. Nielsen, L.V. Roeland, J. Phys. C Solid State Phys. 9 (1976) 1307.
[39] J.-H. Chung, K.H. Lee, Y.-S. Song, T. Suzuki, T. Katsufuji, J. Phys. Soc. Jpn. 82 (2013) 034707.
[40] A. Gukasov, P.J. Brown, J. Phys. Condens. Matter 14 (2002) 8831.
[41] A. Gukasov, P.J. Brown, J. Phys. Condens. Matter 22 (2010) 502201.
[42] H. Cao, A. Gukasov, I. Mirebeau, P. Bonville, C. Decorse, G. Dhalenne, Phys. Rev. Lett. 103 (2009) 056402.
[43] E.A. Klahn, C. Gao, B. Gillon, A. Gukasov, X. Fabreges, R.O. Piltz, S.D. Jiang, J. Overgaard, Chem. Eur. J. 24 (2018) 16576.
[44] I.A. Kibalin, A. Gukasov,Phys. Rev. Res. 1 (2019) 033100. See also https://github.com/ikibalin/cryspy.
[45] R. Baral, D.R. Yahne, M.J. Cochran, M. Powell, J.W. Kolis, H. Zhou, S. Calder, J. Magn. Magn. Mater. 630 (2025) 173342.
[46] I.V. Golosovsky, I.A. Kibalin, A. Gukasov, A.G. Roca, A. López-Ortega, M. Estrader, M. Vasilakaki, K.N. Trohidou, T.C. Hansen, I. Puente-Orench, E. Lelièvre-Berna, J. Nogues, Small Methods 7 (2023) 2201725.
[47] T. Suzuki, T. Katsufuji, J. Phys. Conf. Ser. 150 (2009) 042195.
[48] I.V. Golosovsky, I.A. Kibalin, D. Liguori, B. Muzzi, A.G. Roca, E. Lelièvre-Berna, I. Puente-Orench, A. Gukasov, J. Nogués, A. López-Ortega, Small 22 (2026) e73648.
[49] J.H. Chung, J.H. Kim, S.H. Lee, T.J. Sato, T. Suzuki, M. Katsumura, T. Katsufuji, Phys. Rev. B 77 (2008) 054412.
[50] R.A.P. Ribeiro, S.R. de Lazaro, S.A. Pianaro, J. Magn. Magn. Mater. 391 (2015) 166.
[51] O.V. Nielsen, OJ. Phys. Colloques 32 (1971) C1–C.
[52] H. Si, H. Wang, H. Shen, C. Zhou, S. Li, S. Lou, W. Xu, Z. Du, L.S. Li, CrstEngComm 11 (2009) 1128.
[53] Y. Chen, E. Johnson, E. Peng, J. Am. Chem. Soc. 129 (2007) 10937.
[54] M.A. Roldan, A. Mayence, A. López-Ortega, R. Ishikawa, J. Salafranca, M. Estrader, G. Salazar-Alvarez, M.D. Baró, J. Nogués, S.J. Pennycook, M. Varela, Chem. Eng. J. 405 (2021) 126820.
[55] J. Rodríguez-Carvajal, Phys. B 192 (1993) 55.

[56] T.C. Hansen, P.F. Henry, H.E. Fischer, J. Torregrossa, P. Convert, Meas. Sci. Technol. 19 (2008) 034001.
[57] W. Heil, K. Andersen, D. Hofmann, H. Humblot, J. Kulda, E. Lelievre-Berna, O. Schärpf, F. Tasset, Phys. B 241–243 (1997) 56.
[58] E. Lelièvre-Berna, A.S. Wills, E. Bourgeat-Lami, A. Dee, T. Hansen, P.F. Henry, A. Poole, M. Thomas, X. Tonon, J. Torregrossa, Meas. Sci. Technol. 21 (2010) 055106.